Coherent Multibeam Arrays Using a Cold Aperture Stop

Doug Henke, James Di Francesco, Lewis Knee, and Stéphane Claude

***Abstract*—To increase the mapping speed of a given area-of-sky, multibeam heterodyne arrays may be used. Since typical heterodyne arrays are spatially arranged sparsely at approximately 4·*Nyquist* sampling (i.e., two full-width-half-maximum beam widths), many pointings are required to sample fully the area of interest. A cold aperture stop may be used to increase the packing density of the detectors, which results in a denser instantaneous spatial sampling on-sky. Combining reimaging optics with the cold stop, good aperture efficiency can be obtained. As expected, however, a significant amount of power is truncated at the stop and the surrounding baffling. We analyze the consequence of this power truncation and explore the possibility of using this layout for coherent detection as a multibeam feed. We show that for a fixed area-of-sky, a "twice-Nyquist" spatial sampling arrangement may improve the normalized point source mapping speed when the system noise temperature is dominated by background or atmospheric contribution.**

***Index Terms*—Coherent detectors, cold aperture stop, multibeam array, radio astronomy instrumentation.**

I. Introduction

A. Background

COHERENT multibeam arrays (CMBAs) are arrangements of multiple heterodyne receivers within a single telescope that allow for simultaneous observations of emission from several adjacent locations on the sky. CMBAs are now quite common instruments on single-dish millimeter or submillimeter telescopes [1] and are used for efficient mapping of line emission over sky areas many times their instantaneous on-sky footprints. In general, the wide-field mapping speed of a sparse array increases directly with the number of elements.

One incentive for increased mapping speed is to provide complementary single-dish data to large interferometric arrays, such as the Atacama Large Millimeter/submillimeter Array (ALMA). Although ALMA is impressive in scope, a shortcoming remains its relative insensitivity to large-scale emission. Such emission can be critical to recover so that accurate images are obtained of astrophysical objects. Some measures are in place to allow such emission to be obtained, e.g., through four 12-m total power array antennas [2]. These four single-pixel receiver facilities, however, do not have the same intrinsic sensitivity of ALMA's main array of 50 12-m dishes. To provide effective single-dish data for combination with mosaics, the single-dish observations need to include several on-sky positions sampled at the Nyquist sampling, or better, to preserve all spatial scales from the single-dish beam size up to the size of the map. Therefore, replacing a single-pixel receiver with a CMBA is our motivation.

Manuscript received November 12, 2015; revised March 17, 2016; accepted May 25, 2016. Date of publication June 20, 2016; date of current version July 08, 2016. This work was supported in part by Associated Universities, Inc./National Radio Astronomy Observatory and in part by the National Science Foundation under Cooperative Agreement No. AST-0836064.

D. Henke, J. Di Francesco, and L. Knee are with NRC Herzberg Astronomy and Astrophysics, National Research Council Canada, Victoria, BC V9E 2E7, Canada (e-mail: Doug.Henke@nrc-cnrc.gc.ca; James.DiFrancesco@nrc-cnrc.gc.ca; Lewis.Knee@nrc-cnrc.gc.ca).

S. Claude, deceased, was with the NRC Herzberg Astronomy and Astrophysics, National Research Council Canada, Victoria, BC V9E 2E7, Canada (e-mail: Stephane.Claude@nrc-cnrc.gc.ca).

Color versions of one or more of the figures in this paper are available online at http://ieeexplore.ieee.org.

Digital Object Identifier 10.1109/TTHZ.2016.2576358

B. Modes of Operation for Arrays

With several beams regularly distributed on the sky, CMBAs provide an efficient means for detecting extended astronomical emission. In cases of bright or very extended emission, "on-the-fly" observing techniques may be used. CMBAs may be operated in "raster" or "daisy" modes and continuously swept across areas much larger than their instantaneous footprints, obtaining, respectively, rectangular or circular maps with the Nyquist spatial sampling. In cases of weaker or compact emission, CMBAs can be operated in a "jiggle" mode where they are effectively pointed at a regular series of discrete angular offsets, obtaining small maps of the size of the CMBA footprint across with the Nyquist spatial sampling. Note that while raster scanning techniques obtain fully sampled data, it comes at a cost of overall mapping time, since the continuous angular step size is effectively much smaller compared to a "jiggle" mode.

For the weakest emission, a CMBA can be operated in a "stare" mode with no offsets. Since beam spacings are typically $\sim 2{\cdot}\theta_{\mathrm{FWHM}}$ (where θ_{FWHM} is the full-width-half-maximum of the beam), the Nyquist spatial sampling on the sky is not achieved with this mode.

C. Definitions

To sample fully an area-of-sky (AoS), the Nyquist angular sampling must be achieved. Rectangular or hexagonal sampling may be used, but a hexagonal arrangement fulfills the Nyquist sampling along diagonal paths and is preferred. Using a hexagonal layout [2], the angular on-sky sampling rate is

$$\Delta\theta_{\mathrm{Nyq}} = \theta_{\mathrm{FWHM}}/\sqrt{3} \approx \lambda/\sqrt{3}D \tag{1}$$

where λ is the wavelength and D is the diameter of the primary reflector. When considering the focal plane of the telescope, the hexagonal feed spacing is then

$$\Delta x_{\mathrm{Nyq}} \approx \frac{\lambda}{\sqrt{3}}\frac{f}{D} \quad \Delta y_{\mathrm{Nyq}} \approx \frac{\lambda}{2}\frac{f}{D} \tag{2}$$

where f is the equivalent focal length of the telescope and Δx_{Nyq} and Δy_{Nyq} refer to the horizontal and vertical offset spacing

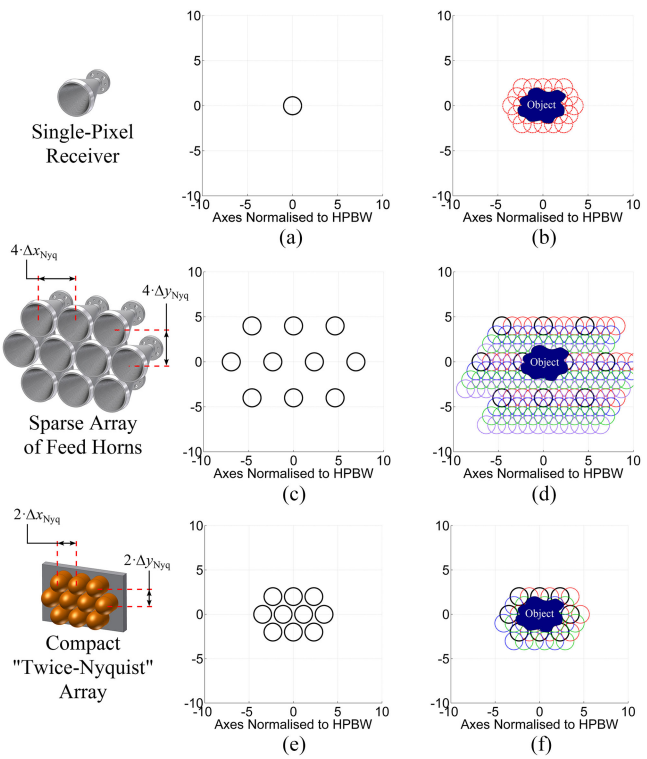

Fig. 1. (a) and (b) Illustrative mosaicing comparison of a single-pixel receiver, (c) and (d) a sparse 4·*Nyquist* array, and (e) and (f) a 2·*Nyquist* array. Assuming a "jiggle" mode and using a single-pixel receiver, the AoS may be imaged by simply pointing as necessary. When a sparse 4·*Nyquist* array is used; however, 16 separate pointings are still required to fill in gaps within the area of interest. If the array spacing is reduced to 2·*Nyquist*, the number of pointings for full sampling is reduced to four.

needed so that the half-power beams overlap for the full Nyquist spatial sampling within a hexagonal layout (see Fig. 1), respectively. Equations (1) and (2) are approximate, since the −3-dB beam width θ_{FWHM} is approximately λ/D on-sky and $\lambda f/D$ at the focal plane.

It is useful to clarify the terms "coherent" and "multibeam." Coherence implies several things, one of which is that a single-mode detector is used [3]. Accordingly, the telescope is limited to a single spatial mode [4], [5] such that the received signal from a point source is a plane wave at the primary reflector rim and is ideally transformed to the focal plane with resolution limited by the Airy pattern. Of course, a strong motivator for coherent signal processing is that high-frequency resolution is possible. Also, within this paper a multibeam array refers to a single optical beam per detector element; it does not refer to a phased array where one beam is synthesized using several elements.

An important theorem which must hold within our analysis is reciprocity. As applied to an antenna, reciprocity implies that the receiving and transmitting radiation patterns are identical for a given mode and polarization as long as the antenna system is linear [6]. Reciprocity will be used to analyze the beam coupling to the telescope and also to evaluate the noise added to the receiver.

II. Consideration of a Cold Aperture Stop

A. Cold Aperture Stop and Analogies From Incoherent Detectors

When considering aperture efficiency and detector spacing, there are analogies between CMBAs and incoherent detectors. One could consider bolometric detectors and CCDs as having very broad transmitting radiation patterns, largely due to the packing density of the detector array. These broad radiation patterns suffer from a considerable amount of inherent spill-over or stray light which is mitigated by the use of shrouds, baffles, and stops (see [7] as one example). Therefore, it is interesting to consider whether or not baffling and stops can be applied effectively to coherent detectors.

We have used the following statement from [1] as motivation for our work.

Closer spacing is possible if the optical system uses more uniform aperture illumination with the detector beam truncated by a cold Lyot stop. This is a typical method for incoherent THz instruments but has not yet been implemented in a coherent array receiver.

In adopting this concept for a CMBA, we have taken the following approach. Baffling should be implemented so that the spill-over power gets terminated without reflection to keep the feeds isolated. Reciprocally, the termination can be thought of as noise power emitted into the receiver, so it is important that its physical temperature is a small fraction of the equivalent receiver noise temperature. By making use of a collimator within the array, a stop may be placed at the point at which all beams coincide, i.e., the *array optical waist* such that each beam is truncated equally [8]. The stop needs to be evaluated (also using reciprocity) to analyze the characteristics of the diffracted beam through the stop and to calculate the resulting single-mode aperture efficiency to validate the coherency of the detector.

B. Feed Spacing and the Detector Array

Various tradeoffs may be made to pack array elements more densely, but generally the diameter of an efficient feed horn limits the closest spacing to $\sim 2 \cdot \theta_{\mathrm{FWHM}}$ [9], [10], resulting in a sparse array, and the telescope is pointed many times to fill in an AoS (e.g., at minimum 16 times for $2{\cdot}\theta_{\mathrm{FWHM}}$ in a "jiggle" mode), as shown in Fig. 1. Without a cold aperture stop, if the feed horn aperture is forced to be smaller to accommodate closer packing density, the resulting beam will simply broaden with respect to the *f/D* of the telescope and be lost as spill-over power.

It is also important that the feed spacing be large enough so that the feeds are isolated (i.e., no mutual coupling). From this perspective, a larger telescope *f/D* is beneficial since the feed element separation scales with *f/D*.

C. Frequency Range and Sampling

A constraint of all arrays is element spacing with respect to frequency bandwidth. To ensure a minimum sampling across the band, the element spacing needs to be determined at the highest frequency, with the outcome that all lower frequencies within the band will be spatially oversampled. This is an important

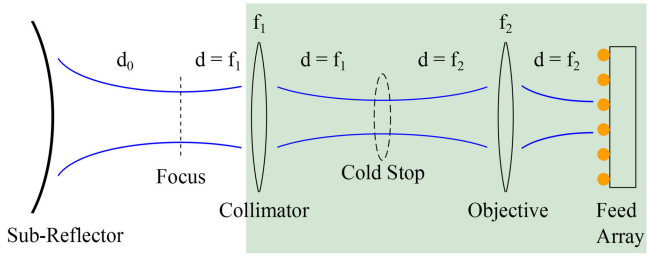

Fig. 2. Simplified unfolded optics demonstrating placement of a cold aperture stop. The shaded area represents cold, absorbing baffling.

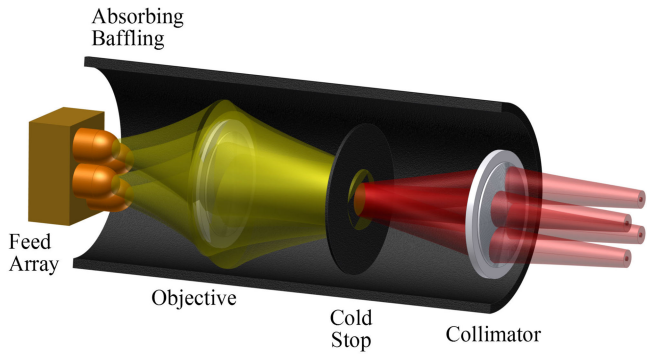

Fig. 3. Illustrative view of reimaging optics used with a cold aperture stop. The feed array is depicted in transmit mode and only four elements are used for clarity.

consequence to arrays and must be considered when considering large bandwidth ratios.

D. Overview of Reimaging Optics

A simplified example of a cold aperture stop implementation is shown in Figs. 2 and 3 where a collimator has been used after the telescope focus and then reimaged onto the detector array.

Baffling is shown by the shaded area in Fig. 2 and represents the region over which any scattered power is terminated by absorber at cryogenic temperature. The beam outside of the shaded area is treated separately as the aperture efficiency of the telescope (see Section II-E).

Note that a more complicated, adjustable reimager could be used to tailor the spacing to the frequency observed, instead of simply fixing the spacing at the highest frequency.

E. Spill-Over Power, Aperture Efficiency, and Noise

Aperture efficiency is a critical metric of the telescope and receiver system and may be determined at various locations along the optical path. Here, we have followed an equivalent paraboloid representation such that the aperture efficiency is evaluated at the rim of the subreflector (see Section III-C) [11], [12].

Given that the feed is placed at the focal plane of the telescope, the aperture efficiency is driven by the feed aperture diameter. For example, if feed aperture diameters are simply reduced to increase the packing density of feeds at the focal plane, a significant amount of power will be lost as spill-over power past the reflector rim. This unacceptable scenario is not the suggestion of this paper. Rather, by reimaging through a cold stop located at the array beam waist, the exiting beam of the cold reimaging optics may be shaped for optimal coupling to the subreflector rim. The cost of the reimaging optics through a cold stop, however, is that signal power is truncated by the stop and baffling. We may separate out the contributions of: 1) the power truncated within the cold absorber baffling and stop of the reimaging optics, and 2) the aperture efficiency of the normalized field, which exits the reimaging optics and is evaluated at the rim of the subreflector.

To emphasize this point, it is the normal approach that when no cold stop is used, the aperture efficiency calculation includes signal truncation along the entire optical path as it is already represented within the spill-over term. Here, however, we specifically separate out two main contributions of spill-over for a feed coupled to a telescope: 1) spill-over power which is intercepted by the cold aperture stop and baffling, here referred to as *truncated signal power* and 2) spill-over of the normalized signal which exits the reimaging optics and is calculated with respect to the subreflector rim, here presented as part of the aperture efficiency.

Our intent is to analyze the noise consequence of the truncated power within the cryogenic baffling/cold stop and to demonstrate that high aperture efficiency, of the signal which exits the reimaging optics, can be achieved by choosing the appropriate cold stop diameter.

TABLE I
OPTICAL SYSTEM UNDER CONSIDERATION

Subreflector	Cassegrain Focus	Collimator	Stop	Objective	Detector Array
Distances with respect to Focus (mm)					
−6000.0	0.0	157.8	315.6	473.4	631.2

III. ANALYSIS PROCEDURE

A. Design Parameters for the Optical System

It is useful to consider the example frequency of ALMA Band 3 (84–116 GHz) using design parameters taken from the ALMA telescope [2], [11], [13].

In [14], a comparison of two types of fully Nyquist-sampled detector arrays was shown. It was concluded there that a 1·*Nyquist* array of modest size offered no benefit compared to a single-pixel receiver because of the severe degradation to overall receiver noise. Within this paper, we explore widening the array spacing to 2·*Nyquist* (still very compact). Details of the analysis procedure are given in [14] and a summary is provided below.

Using quasioptics [15], design parameters of the reimaging optics may be found using ideal beam characteristics and working backward from the subreflector, assuming that the edge taper and focus are constant over frequency when evaluated at the subreflector. Given the layout described in Fig. 2, the design is summarized in Table I.

In this design, the distance between the focal plane and subreflector is assumed to be 6 m and distances are given with respect to the focal plane in the direction toward the detector array. Note that the reimaging system used within this document has $f/D = 1$.

B. Simulation Procedure

The array feeds were simulated within CST Microwave Studio to analyze the reflected power and isolation of the ports. The embedded near-fields were then exported into GRASP (preserving the axial offset of the feeds) to simulate the reimaging optics and then projected onto the telescope reflector to evaluate beam quality, resulting spacing, and aperture efficiency (see [14] for additional details).

To keep the discussion simple, only axially aligned mirrors were used, as is possible only in simulation. For a more realistic simulation, off-axis folded mirrors or on-axis lenses would be required, and the associated distortion and cross-polarization would degrade the simulated aperture efficiency.

Within GRASP, an ideal absorbing surface was defined for the absorbing aperture stop. Since the aperture diameter of the cold stop is electrically small for physical optics simulations, a comparison was made using CST to confirm the predictions. The near-field of an on-axis Gaussian signal was simulated through a 3-D model of a cold stop using CST and found to agree with the results from GRASP.

C. Aperture Efficiency

The aperture efficiency was calculated using an overlap integral [11], [12], at the rim of the subreflector with respect to the focal plane of the telescope. Following [11], an equivalent paraboloid representation was used such that the total aperture efficiency η_{total} may be broken up into the individual products of spill-over, polarization, amplitude, and phase efficiencies and calculated, respectively, as

$$\eta_{\text{spill}} = \frac{\int_0^{2\pi}\int_0^{\theta_m}\left(|\boldsymbol{E}_{\text{co}}|^2 + |\boldsymbol{E}_{\text{cross}}|^2\right)\sin\theta\, d\theta d\phi}{\int_0^{2\pi}\int_0^{\pi}\left(|\boldsymbol{E}_{\text{co}}|^2 + |\boldsymbol{E}_{\text{cross}}|^2\right)\sin\theta d\theta d\phi} \tag{3}$$

$$\eta_{\text{pol}} = \frac{\int_0^{2\pi}\int_0^{\theta_m}\left(|\boldsymbol{E}_{\text{co}}|^2\right)\sin\theta d\theta d\phi}{\int_0^{2\pi}\int_0^{\theta_m}\left(|\boldsymbol{E}_{\text{co}}|^2 + |\boldsymbol{E}_{\text{cross}}|^2\right)\sin\theta d\theta d\phi} \tag{4}$$

$$\eta_{\text{amp}} = \frac{\left[\int_0^{2\pi}\int_0^{\theta_m}\left(|\boldsymbol{E}_{\text{co}}|\right)\sin\theta d\theta d\phi\right]^2}{\left[\int_0^{2\pi}\int_0^{\theta_m}\left(|\boldsymbol{E}_{\text{co}}|^2\right)\sin\theta d\theta d\phi\right]\cdot\left[\int_0^{2\pi}\int_0^{\theta_m}\sin\theta d\theta d\phi\right]} \tag{5}$$

$$\eta_{\text{phase}} = \left[\frac{\left|\int_0^{2\pi}\int_0^{\theta_m}\left(\boldsymbol{E}_{\text{co}}\right)\sin\theta d\theta d\phi\right|}{\int_0^{2\pi}\int_0^{\theta_m}\left(|\boldsymbol{E}_{\text{co}}|\right)\sin\theta d\theta d\phi}\right]^2 \tag{6}$$

where θ_m is the opening half-angle of the subreflector and $\boldsymbol{E}_{\text{co}}$ and $\boldsymbol{E}_{\text{cross}}$ are, respectively, the co- and cross-polarized electric fields projected onto a spherical grid. To ensure that the phase is referred to the telescope focus, the origin of the spherical grid is set at the focal plane of the telescope and the reference distance taken as the distance between the focal plane and rim of the subreflector.

Note that the scattered or intercepted power between the feed array and collimator (i.e., power that is absorbed by the cold stop and baffling) was not included within this calculation. Only the field exiting the cryostat was used and normalized accordingly.

D. Consequence of the Cold Stop to Receiver Noise

It is essential to determine how to treat the power that is truncated by the baffling and aperture stop, since the dense feeds have very broad radiation patterns. Using GRASP, the array feed element may be excited to calculate the amount of cumulative intercepted signal power within the shaded region of Fig. 2. When considering the transmitting case, the amount of signal power received at the output of the collimator, is also, by reciprocity, the amount of signal power coupled into the feed with respect to the input of the cryostat (i.e., input to the cold reimaging optics). Likewise, the power truncated by the surrounding cold absorber is treated as noise power added into the feed.

The truncated power intercepted by the cold stop and baffling can be quantified in terms of a cascaded receiver noise analysis and the resulting overall receiver noise $T_{o\text{Rec}}$ can be found using the standard *Y-factor* technique where the input hot/cold noise temperature to the receiver is replaced by

$$T_{\text{in},h/c} = T_{h/c}\eta_{\text{coupling}} + T_{\text{baffle}}\left(1 - \eta_{\text{coupling}}\right) \tag{7}$$

where $T_{h/c}$ is the input hot or cold noise temperature of the calibration load presented to the overall receiver (i.e., input of the cryostat window) used to determine the power *Y-factor*. T_{baffle} is the physical temperature of the baffling and cold stop assuming ideal blackbody radiation, η_{coupling} is the fraction of power that is coupled into each detector element (i.e., $1 - -\eta_{\text{coupling}}$ is truncated by the cold stop and baffling), and T_{rec} is the equivalent noise temperature of the receiver (i.e., the receiver noise of each element within the detector array not including the effects of the cold stop and baffling). From the *Y-factor*

$$Y = \frac{T_{\text{in},h} + T_{\text{rec}}}{T_{\text{in},c} + T_{\text{rec}}} \tag{8}$$

the overall receiver noise is then

$$T_{o\text{Rec}} = \frac{T_h - YT_c}{Y - 1} = \frac{T_{\text{rec}} + T_{\text{baffle}}\left(1 - \eta_{\text{coupling}}\right)}{\eta_{\text{coupling}}}. \tag{9}$$

Fig. 4 illustrates the consequence to overall receiver noise when the truncated signal power is terminated by various baffle and stop temperatures T_{baffle}. One can see directly that the aperture stop and baffling must be held at cryogenic temperatures to avoid a substantial increase in overall receiver noise. In the example shown in Fig. 4, it is assumed that the receiver element has an equivalent noise temperature of 35 K, representative of the ALMA B3 receiver cartridge [16].

A cold aperture stop with reimaging optics allows the designer to choose arbitrary detector feed spacings. Depending on the compactness of the detector array, however, the amount of truncated power will change. For example, wider

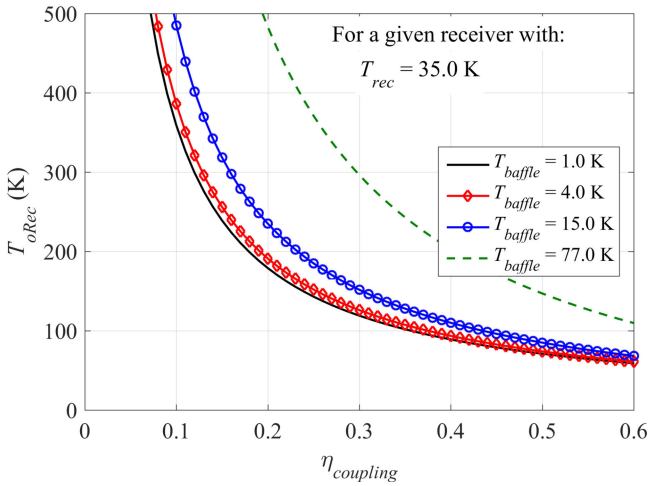

Fig. 4. Effect of signal coupling into the detector feed when the truncated signal is terminated by the cold aperture stop and absorbing baffling is held at different physical temperatures.

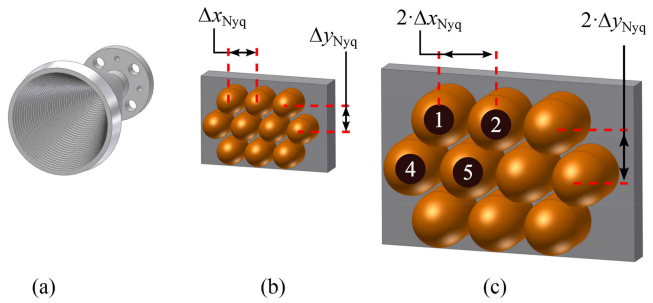

Fig. 5. Feed models showing (a) a single-pixel feed horn (from which a constructed array would be limited to 4·*Nyquist* and shown for scaling reference), (b) a compact array with Nyquist sampling, and (c) a compact array with twice-Nyquist sampling. Array feed element numbers are shown in (c).

spacings allow for larger feed diameters, improving directivity and implying that η_{coupling} will be closer to unity (see Section IV-C).

IV. Discussion and Results

A. Feed Models

Given the large amount of signal power truncation that resulted from a fully sampled Nyquist-spaced array shown in [14], it is interesting to consider here the improvement when the array spacing is widened to 2·*Nyquist*, as shown in Fig. 5.

For simplicity, the lenslets of each array were kept to have the same input circular waveguide and the lenslet diameter was set to give a 1-mm clearance between lenslets. For each case, a single lenslet was optimized for beam quality and input reflection. Next, the entire array was simulated in CST Microwave Studio to ensure that port reflection <-20 dB and port isolation <-30 dB. Note that no preference is made here between small-aperture waveguide horns and lenslets. Either feed element type may be used within a compact array (e.g., Nyquist or twice-Nyquist spacing) provided they are designed with equivalent characteristics.

B. Copolar Far-Fields On-Sky

Each port's near-field was exported to GRASP and analyzed through the optical path to compute the far-fields at the subreflector of the telescope. Fig. 6 shows the -3-dB contours of the simulated far-fields of each array model. The FWHM contours at 116 GHz agree with the predicted spatial sampling and a high degree of symmetry is evident between all off-axis detector beams, indicating that the aperture stop is located properly.

Fig. 6 is also useful to emphasize that element spacing is fixed by the highest frequency within the band such that lower frequencies in the band are oversampled.

C. Signal Power Coupled to Each Feed

The change in signal power coupling is of interest for each case shown in Fig. 5(b) and (c). Using a transmitting mode, Table II summarizes the cumulative fractional power evaluated along the optical path, relative to the element feed excitation, for each array considered. The final column in Table II is the fraction of power which exits the cold reimaging optics and, by reciprocity, is also the value of η_{coupling}. In (b), significant improvement is shown when using twice-Nyquist sampling. Note that there is some variation in the result for the less dense, larger array, most likely due to the fixed size of the optics and possible edge effects within the array. Increasing the size of the optics and adding a buffer ring of array elements terminated within the waveguide may mitigate these variations.

Following (7)–(9), the resulting overall receiver noises can be plotted for the two array spacing cases and are shown in Fig. 7. It is interesting to note the shift along the curve for twice-Nyquist spacing and that there is less spread in the overall receiver noise across frequency.

D. Calculated Aperture Efficiency

The aperture stop radius was set to 11 mm (found to optimize the aperture efficiency) and the resulting field exiting the cryostat was plotted with respect to a normalized feed power of 4π. Using the fourth feed port (most off-axis), the aperture efficiencies from each array were calculated using (3)–(6) and are shown in Table III. An equivalent paraboloid was used, following [11], and the subreflector rim was represented as subtending an opening half-angle of 3.58°, as in ALMA 12-m antennas.

As mentioned earlier, since the optics were simplified as on-axis mirrors and an equivalent paraboloid was used, the computed polarization efficiency is ideal and has been included for completeness.

It is important to note that the aperture stop is a Lyot stop. By stopping the field at the array optical waist, the resulting transform to the focal plane is essentially an Airy pattern. Hence, the resulting beams efficiently illuminate the subreflector. In fact, Table III demonstrates that by choosing the correct aperture stop diameter, the aperture efficiency of each array element can

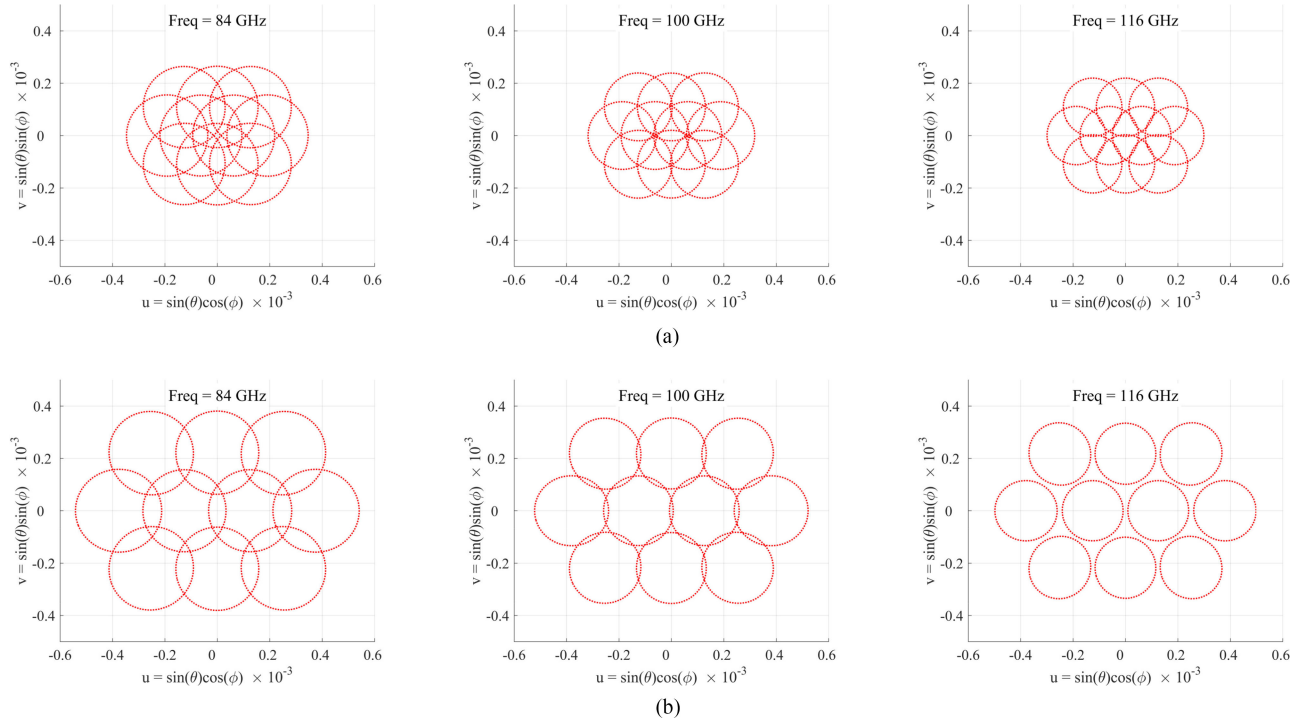

Fig. 6. Simulated FWHM contours of the co-polar far-field on-sky projections for each feed port using element spacing corresponding to (a) Nyquist and (b) twice-Nyquist. The element spacing has been fixed according to the highest frequency of 116 GHz, which results in oversampling at lower frequencies. (a) Nyquist, $\Delta x_{\mathrm{Nyq}} = 11.94$ mm and (b) twice-Nyquist, $2 \cdot \Delta x_{\mathrm{Nyq}} = 23.88$ mm.

TABLE II
CUMULATIVE FRACTIONAL POWER ALONG THE OPTICAL PATH, FOR A TRANSMITTING MODE RELATIVE TO THE FEED ELEMENT EXCITATION, AND GIVEN FOR EACH ARRAY MODEL WITH SPACING: (A) NYQUIST AND (B) TWICE-NYQUIST. NOTE THAT η_{coupling} IS THE CUMULATIVE FRACTIONAL POWER WHICH EXITS THE COLD REIMAGING OPTICS AND, BY RECIPROCITY, THIS IS THE AMOUNT OF SIGNAL POWER COUPLED TO THE DETECTOR FEED.

Cumulative Fractional Power Lenslet Diameter = 10.94 mm, Δx_{Nyq} = 11.94 mm					
Frequency	Feed Element	Objective	Stop	Collimator	$\eta_{coupling}$
84 GHz	**1**	66.8%	54.8%	11.1%	10.1%
	2	65.4%	54.1%	10.5%	9.6%
	4	68.1%	56.2%	10.9%	9.9%
	5	60.9%	50.1%	10.1%	9.1%
100 GHz	**1**	78.7%	61.9%	15.8%	14.4%
	2	78.2%	61.5%	15.8%	14.4%
	4	78.3%	62.0%	15.4%	14.0%
	5	75.7%	59.8%	15.1%	13.7%
116 GHz	**1**	83.3%	61.6%	20.7%	18.9%
	2	83.5%	61.7%	20.9%	19.1%
	4	83.6%	62.0%	20.6%	18.8%
	5	80.4%	59.2%	20.4%	18.6%

(a)

Cumulative Fractional Power Lenslet Diameter = 22.88 mm, $2{\cdot}\Delta x_{Nyq}$ = 23.88 mm					
Frequency	Feed Element	Objective	Stop	Collimator	$\eta_{coupling}$
84 GHz	**1**	70.4%	39.7%	28.7%	26.4%
	2	68.8%	36.3%	30.6%	28.3%
	4	70.0%	40.6%	27.3%	25.0%
	5	67.6%	35.2%	30.6%	28.3%
100 GHz	**1**	77.3%	39.2%	36.3%	33.7%
	2	77.7%	35.8%	40.2%	37.4%
	4	77.2%	43.0%	32.1%	29.7%
	5	75.8%	32.2%	42.1%	39.3%
116 GHz	**1**	82.2%	34.6%	45.7%	42.8%
	2	81.5%	29.8%	50.1%	47.0%
	4	83.0%	37.2%	43.6%	40.6%
	5	81.8%	27.6%	52.7%	49.6%

(b)

be as efficient as single-pixel feeds. More detailed field plots along the optical path are shown in [14].

E. Comparison of Point Source Mapping Speed for Sparse and Twice-Nyquist Arrays

Here, we compare the mapping speed between a sparse and twice-Nyquist array for a given fixed AoS. Within a fixed AoS, a twice-Nyquist array will have four times the number of elements as a sparse array within the same array footprint. So we ask whether or not placing these noisier elements in a denser configuration will improve overall array mapping time to get a fully sampled image.

We propose that within a fixed AoS, and compared to a sparse array, a twice-Nyquist array with a cold aperture stop *may* improve the relative mapping speed for a fully sampled AoS—it depends on the amount of background and sky noise contribution within T_{sys}. We consider the example of ALMA Band 3 to illustrate the point.

We assume here that the beams within a sparse array are the same as that of an efficient single-pixel receiver and thus do not require a cold aperture stop. For simplicity, we assume that the

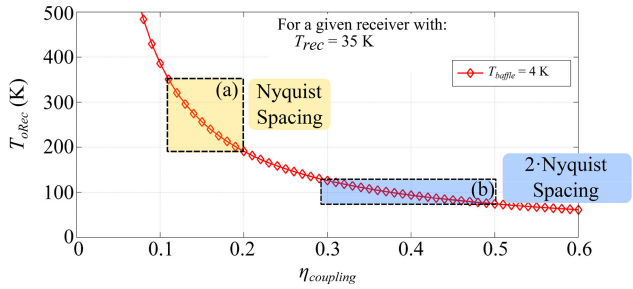

Fig. 7. Overall receiver noise for the array models shown in Fig. 5. The shaded boxes indicate the region of the curve that is covered across the frequency range of 84–116 GHz corresponding to Table II, where (a) and (b) have Nyquist and twice-Nyquist element spacing, respectively. It is assumed that the absorber is held at a temperature of 4 K and that the receiver noise, without including the effects of the truncated power, is 35 K.

TABLE III
CALCULATED APERTURE EFFICIENCY FOR THE MODELS OF FIG. 5 (B) AND (C) USING THE FOURTH FEED PORT AND AN OPENING HALF-ANGLE OF 3.58°

Frequency (GHz)	Feed Element	η_{spill}	η_{amp}	η_{pol}	η_{phase}	η_{total}
84	4th (1·Nyq)	0.892	0.985	1.000	0.991	0.871
100		0.894	0.990	1.000	0.990	0.876
116		0.898	0.990	1.000	0.991	0.882
84	4th (2·Nyq)	0.894	0.949	1.000	0.992	0.842
100		0.895	0.912	1.000	0.993	0.810
116		0.908	0.935	1.000	0.989	0.839

number of sidebands and polarizations are the same throughout (although to the authors' knowledge, no existing heterodyne array simultaneously achieves two sidebands, two orthogonal polarizations, and 4·*Nyquist* spacing). Furthermore, effects of oversampling due to frequency bandwidth (as shown in Fig. 6) are not included.

For a point source, the integration time for a given signal-to-noise ratio is proportional to $(A_e/T_{\rm sys})^2$, where A_e is the aperture efficiency and $T_{\rm sys}$ is the system noise temperature of the receiver elements.

To determine the mapping speed of an extended source, the source coupling efficiency should technically be used instead of the aperture efficiency [15]. It is still convenient, however, to simplify the analysis and use aperture efficiency to compare array mapping speeds. To distinguish this simplification, we use the term *point source mapping speed*. We compare the point source mapping speed of a single-pixel receiver, a sparse array (i.e., 4·*Nyquist* spacing) with no cold stop, and a twice-Nyquist array with a cold stop.

From [2], neglecting background terms and pointing at zenith, the system temperature is

$$T_{\rm sys} = \frac{1}{\eta_{\rm eff}\, e^{-\tau_0}} \left(T_{o\rm Rec} + \eta_{\rm eff} T_{\rm sky} + (1-\eta_{\rm eff})\, T_{\rm amb}\right) \quad (10)$$

where $T_{o\rm Rec}$ is the overall receiver noise, $\eta_{\rm eff}$ is the forward efficiency (fixed at 0.95 in [2]), $e^{-\tau 0}$ is the fractional transmission of the atmosphere at zenith, $T_{\rm sky}$ is the sky temperature, and $T_{\rm amb}$ is the ambient temperature (fixed at 270 K in [2]).

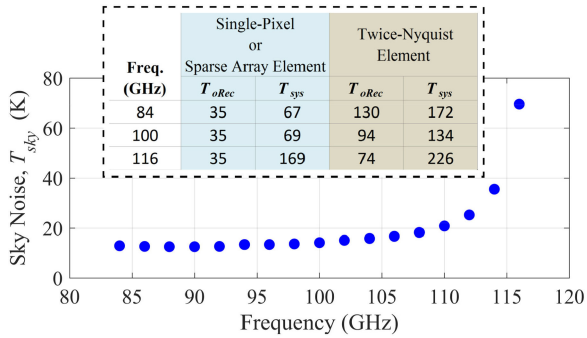

Fig. 8. Assumed values of sky noise temperature using values found with the ALMA Sensitivity Calculator for ALMA Band 3 with a zenith water vapor column density of 5.1 mm. The corresponding system noise temperatures $T_{\rm sys}$ are shown within the inset and have been calculated according to (10).

Using the ALMA Sensitivity Calculator (ASC),[1] values of sky temperature and atmospheric transmission can be found and are shown in Fig. 8. We assume nominal observing conditions for ALMA Band 3, i.e., a water vapor column density of 5.1 mm.

Using the values of $T_{\rm sky}$ along with (10), the system noise temperatures $T_{\rm sys}$ of a characteristic single-pixel receiver and an element within a twice-Nyquist array can be computed. These values of $T_{\rm sys}$ will be used as part of the point source mapping speed and are shown within the inset of Fig. 8. Again, we assume that the sparse array receivers (i.e., 4·*Nyquist* spacing) achieve the same $T_{\rm sys}$ as a single-pixel receiver.

The point source mapping speed figure of merit for a fixed AoS is

$$MS_{\rm ps,AoS} = \frac{1}{N_{p,\rm AoS}} \cdot \left(\frac{A_e}{T_{\rm sys}}\right)^2 \quad (11)$$

where $N_{p,AoS}$ is the number of pointings to sample fully the particular AoS. Consider a simple example of a grid map shown in Fig. 9. It takes 64 pointings with a single beam, 16 pointings with a 2 × 2 sparse array, or 4 pointings with a 4 × 4 twice-Nyquist array.

One may then find the *normalized* point source mapping speed for a particular AoS with respect to a single-pixel receiver

$$MS_{\rm ps,AoS} = \frac{MS^{\rm Array}_{\rm ps,AoS}}{MS^{\rm Single-Pixel}_{\rm ps,AoS}} = \frac{N^{\rm Single-Pixel}_{p,\rm AoS}}{N^{\rm Array}_{p,\rm AoS}} \left(\frac{T^{\rm Single-Pixel}_{\rm sys}}{T^{\rm Array}_{\rm sys}}\right)^2 \quad (12)$$

Note that aperture efficiency is assumed to cancel in (12) since, as shown earlier, single-pixel, sparse array, and twice-Nyquist array beams can have comparable aperture efficiencies. $T_{\rm sys}$ has been shown within the inset of Fig. 8 for both sparse and twice-Nyquist arrays.

We may extend the example for successively larger AoS maps using an 8 × 8, 12 × 12, or 16 × 16 grid maps; in each case, the corresponding sparse array footprint is 2 × 2, 3 × 3, or 4 × 4, respectively. Table IV shows the details of each AoS and the normalized point source mapping speed calculated using (12).

[1][Online]. Available: https://almascience.nrao.edu/proposing/sensitivity-calculator

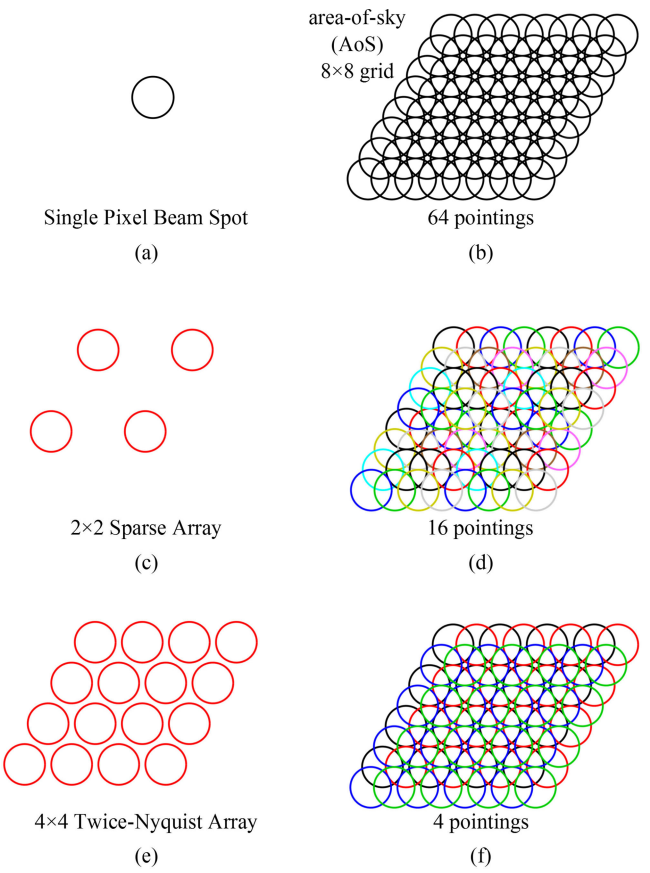

Fig. 9. Illustration of an example AoS formed by 16 pointings of a 2×2 sparse array. The fully sampled grid may be mapped using: (a) and (b) a single-pixel receiver with 64 pointings; (c) and (d) a 2×2 sparse array with 16 pointings; or, (e) and (f) a 4×4 twice-Nyquist array with 4 pointings.

TABLE IV
COMPARISON OF NORMALIZED POINT SOURCE MAPPING SPEEDS OF TWICE-NYQUIST AND SPARSE ARRAYS WITH RESPECT TO A SINGLE-PIXEL RECEIVER: (A) SHOWS THAT EACH AOS HAS BEEN CHOSEN TO CORRESPOND WITH A RECTANGULAR SPARSE ARRAY OF 2×2, 3×3, OR 4×4 ELEMENTS; (B) INDICATES THE NUMBER OF POINTINGS FOR FULL SAMPLING; AND (C) SHOWS THE CALCULATED NORMALIZED POINT SOURCE MAPPING SPEED

	Array Size		
AoS Grid of Points	Single-Pixel Receiver	Sparse Array	Twice-Nyquist Array
8×8	**1**	**2×2**	**4×4**
12×12	**1**	**3×3**	**6×6**
16×16	**1**	**4×4**	**8×8**

(a)

	Minimum Number of Pointings, N_p		
AoS Grid of Points	Single-Pixel Receiver	Sparse Array	Twice-Nyquist Array
8×8	**64**	**16**	**4**
12×12	**144**	**16**	**4**
16×16	**256**	**16**	**4**

(b)

	Normalized Point Source Mapping Speed				
			Twice-Nyquist Array		
AoS Grid of Points	Single-Pixel Receiver	Sparse Array	84 GHz	100 GHz	116 GHz
8×8	**1**	**4.0**	**2.4**	**4.2**	**8.9**
12×12	**1**	**9.0**	**5.5**	**9.4**	**20.0**
16×16	**1**	**16.0**	**9.7**	**16.8**	**35.6**

(c)

Consider the normalized point source mapping speed for the sparse arrays, shown in the center column of Table IV(c). As expected, the sparse array mapping speeds improve proportional to the number of elements, e.g., a 2×2 sparse array increases the normalized point source mapping speed by a factor of 4, a 3×3 sparse array increases the speed by nine times, etc.

What happens for the corresponding twice-Nyquist array that contains four times as many elements as the sparse array? Using the example of ALMA Band 3 is interesting because the sky noise changes significantly over the band, as shown in Fig. 8, due to water and oxygen absorption lines. At 84 GHz, the twice-Nyquist array will actually take longer to map the same AoS than a sparse array—despite having four times as many elements and only needing 4 pointings. This leads to the generally held notion that arrays cannot be made to map more efficiently by simply increasing their packing density past a sparse array layout.

There are two mechanisms at 84 GHz which make the mapping speed worse: 1) the beams at the cold aperture stop are largest at the lowest frequency and therefore more power is truncated by the stop and 2) the contribution of the background and sky noise is not as significant with respect to the single element receiver noise.

Next, looking at 100 GHz, the normalized point source mapping speeds for the sparse and twice-Nyquist arrays are essentially the same. Compared to 84 GHz, the amount of background and sky noise contribution is approximately the same at 100 GHz, but the beam size is narrower at the cold stop for 100 GHz, so less power is truncated and the corresponding $T_{\rm sys}$ of the twice-Nyquist element is less. Still, the twice-Nyquist array at 100 GHz may not appear worthwhile since four times as many elements are required for the same mapping performance compared to a sparse array.

At 116 GHz, however, the situation changes since the beams are narrowest at the cold stop and the background noise contribution is much more significant. In fact, the mapping efficiency of the twice-Nyquist array is doubled compared to a sparse array, and in this scenario, it may actually be worth the added complexity to implement a twice-Nyquist layout.

Therefore, the design trade-off of which type of array to use is aptly illustrated using the example of ALMA Band 3. In the lower half of the band, a sparse array is the clear winner. Across the upper half of the band, however, a twice-Nyquist array will provide superior point source mapping speed compared to a sparse array, for the same AoS.

V. FUTURE WORK

Using a twice-Nyquist detector layout creates a major challenge to fit all of the receiver chain components within the

volume. Retaining both linear polarizations and sideband-separation makes the problem even more challenging since for each feed element, four outputs are needed. One possibility would be to use an input turnstile as the first stage of a compact sideband separating assembly [17].

Many system issues, such as available interfaces, cryogenic cooling capacity, LO power, cabling, de-rotation, back-end requirements, and telescope slew rate, have not been considered herein and further study is required.

VI. Conclusion

An optical layout has been presented to explore the ramifications of full spatial sampling with multibeam feeds using dense hexagonal element spacings. A cold aperture stop with reimaging optics enables the designer to reduce the element spacing while still achieving good aperture efficiency. The truncated signal power into the absorbing stop and baffling, however, will degrade the overall receiver noise.

To show the impact on mapping efficiency, a comparison between sparse and twice-Nyquist arrays was presented using normalized point source mapping speed.

The example of the ALMA Band 3 receiver was shown to be illustrative since the ratio of receiver to system noise changes substantially across the frequency band.

Notwithstanding system complexity, the design choice of which array to use should be made on the dominance of receiver noise within system noise, which varies depending on the frequency and site location. When the system noise is dominated by atmospheric or background contribution, increasing the element packing density using a twice-Nyquist layout will improve the point source mapping speed compared to a sparse array, for a given AoS. Conversely, if atmospheric contributions are low, then a sparse array with no cold stop will outperform a twice-Nyquist array, for a given AoS.

VII. Dedication

The authors would like to remember their dear colleague, S. Claude. Stéphane had a profound impact on those who knew him, and his passion for life was felt by his family, friends, and colleagues. He was both mentor and friend: a mentor because he was encouraging during learning, took joy in successes, and believed in the talents and abilities of those around him; a friend because he cared about the personal interests of others, found common ground, and enthusiastically shared his own experiences. The memory of Stéphane continues to inspire those who knew him.

Acknowledgment

The authors would like to thank J. Atwood and J. Pazder for helpful conversations about optics fundamentals and T. Hardy and J.-P. Veran for informative discussions of optical detectors.

References

[1] C. E. Groppi and J. H. Kawamura, "Coherent detector arrays for terahertz astrophysics applications," *IEEE Trans. THz Sci. Technol.*, vol. 1, no. 1, pp. 85–96, Sep. 2011.

[2] A. Lundgren, "ALMA Cycle 2 Technical Handbook," ver. 1.1, 2013. [Online]. Available: http://www.almascience.org

[3] J. Lesurf, *Millimetre-Wave Optics, Devices System*. England, U.K.: IOP, 1990.

[4] J. Murphy and R. Padman, "Focal-plane and aperture-plane heterodyne array receivers for millimeter-wave radioastromony—A comparison," *Int. J. Infrared Millim. Waves*, vol. 9, no. 8, pp. 667–704, Aug. 1988.

[5] P. F. Goldsmith *et al.*, "Focal plane imaging systems for millimeter wavelengths," *IEEE Trans. Microw. Theory Techn.*, vol. 41, no. 10, pp. 1664–1675, Oct. 1993.

[6] C. A. Balanis, *Antenna Theory: Analysis and Design*, 2nd ed. New York, NY, USA: Wiley, 1997.

[7] J. Glenn *et al.*, "Current status of Bolocam: A large-format millimeter-wave bolometer camera," *Proc. SPIE*, vol. 4855, pp. 30–40, Feb. 2003.

[8] B. Weiner, "Scaling relations for telescopes, spectrographs, and reimaging instruments. Stewart Observatory," University of Arizona, Tuscon, AZ, USA. Sep. 2008. [Online]. Available: http://mingus.as.arizona.edu/∼bjw/spectrographs/spectrographs.pdf

[9] P. F. Goldsmith, "Focal plane arrays for millimeter-wavelength astronomy," in *IEEE MTT-S Int. Microw. Symp. Dig.*, vol. 3, Jun. 1992, pp. 1255–1258.

[10] R. Padman, "Optical fundamentals for array feeds," in *Proc. Multi-Feed Syst. Radio Telesc., ASP Conf.*, vol. 75, 1995, pp. 3–26.

[11] K. Pontoppidan, "Electromagnetic properties and optical analysis of the ALMA antennas and front ends," Nat. Radio Astron. Observatory, Charlottesville, VA, USA, ALMA EDM Doc. FEND-80.04.00.00-026-A-REP, Jan. 2008.

[12] J. W. Lamb, "Low-noise, high-efficiency optics design for ALMA receivers," *IEEE Trans. Antennas Propag.*, vol. 51, no. 8, pp. 2035–2047, Aug. 2003.

[13] M. Carter *et al.*, "ALMA front-end optics design report," Nat. Radio Astron. Observatory, Charlottesville, VA, USA, ALMA EDM Doc. FEND-40.02.00.00-035-B-REP, Jul. 2007.

[14] D. Henke, S. Claude, and J. Di Francesco, "Full sampling using a dense hexagonal array of coherent multi-beam detectors," in *Proc. 26th Int. Symp. Space THz Technol.*, W2-1, pp. 1–6, Mar. 16–18, 2015.

[15] P. F. Goldsmith, *Quasioptical Systems: Gaussian Beam Quasioptical Propagation and Applications*. New York, NY, USA: IEEE Press, 1998.

[16] S. Claude *et al.*, "Performance of the production band 3 receivers (84–116 GHz) for the atacama large millimeter array (ALMA)," *Int. J. Infrared Millim. Waves*, vol. 35, no. 6/7, pp. 563–582, Jul. 2014.

[17] D. Henke, "A Compact Sideband-Separating (2SB) Arrangement using a Turnstile," in *Proc. Int. Conf. Electromagn. Adv. Appl.*, Turin, Italy, Sept. 7–11, 2015, pp. 468–471.

Doug Henke received the B.Eng. and M.A.Sc. degrees in electrical engineering from the University of Victoria, Victoria, BC, Canada, in 2001 and 2005, respectively.

From 2006 to 2009, he was a Research Engineer with the Group for Advanced Receiver Technology, Chalmers University of Technology, Gothenburg, Sweden, and participated in the development of the Swedish Heterodyne Facility Instrument installed at the APEX telescope. Currently, he is a Research Engineer with the Millimetre Instrumentation Group, NRC Herzberg Astronomy and Astrophysics, Victoria, BC, Canada. His research interests include the development of low-noise cryogenic receivers used in radio astronomy; including the EM modeling, SIS mixers, waveguide component development, mechanical design, multibeam arrays, phased-array feeds, and millimeter-wave optics.

James Di Francesco received the B.Sc. degree in physics and astronomy from the University of Toronto, Toronto, ON, Canada, in 1990, and the Ph.D. degree in astronomy from The University of Texas at Austin, Austin, TX, USA, in 1997.

From 1997 to 1999, he was an SAO Postdoctoral Fellow with the Harvard-Smithsonian Center for Astrophysics. From 1999 to 2002, he was a BIMA Fellow with the Radio Astronomy Laboratory, University of California, Berkeley. Since 2002, he has been an Astronomer with the Millimetre Astronomy Group, National Research Council's Herzberg Programs in Astronomy and Astrophysics,Victoria, BC, Canada. His role at NRC has included support of North American involvement in the international Atacama Large Millimetre Array (ALMA) Project. He is also an Adjunct Associate Professor with the Department of Physics and Astronomy, University of Victoria, Victoria, BC, Canada. His scientific interests include the observational characterization of the earliest phases of star formation in the Galaxy, typically using instruments that detect emission at far-infrared to radio wavelengths. His technical interests include the development of multifeed focal-plane arrays for radio/millimeter telescopes.

Lewis Knee received the B.Sc. degree in physics from the Memorial University of Newfoundland, St. John's, NL, Canada, in 1983, the M.Sc. degree in astronomy from the University of Victoria, Victoria, BC, Canada, in 1985, and the Ph.D. degree in radio and space science from the Chalmers University of Technology, Gothenburg, Sweden, in 1991.

From 1992 to 1996, he was a Postdoctoral Fellow with the Swedish-ESO Submillimetre Telescope, Chile. In 1996, he joined the National Research Council of Canada, working both with the Dominion Radio Astrophysical Observatory, Penticton, BC, Canada, and with the Dominion Astrophysical Observatory (DAO), Victoria, BC, Canada. From 2004 to 2007, he was the Head of the Millimetre Astronomy Group, DAO, and from 2008 to 2013, he was the System Integration Science Team Leader at the Joint ALMA Observatory, Chile. In 2014, he was an Appointed Team Leader of the Millimetre Instrumentation Group, DAO. His scientific interests include radio and (sub)millimeter observational studies of star formation, mass outflows in young stellar objects, and the structure and evolution of the atomic and molecular components of the interstellar medium of the Galaxy. His technical interests include radio telescope operations and the commissioning of single dish and interferometric radio astronomy systems.

Stéphane Claude (deceased September 2014) received the Engineering degree in material sciences from the École Nationale Supérieure d'Ingénieurs de Caen, Caen, France, in 1990, and the Ph.D. degree in physics from London University, Queen Mary, and Westfield College, London, U.K., in 1996.

From 1990 to 1996, he was a Research Associate with the Rutherford Appleton Laboratory, Chilton, U.K., where he developed techniques for the fabrication of superconducting–insulator–superconducting mixer chips for low-noise submillimeter receivers in radio astronomy. His doctoral research was to commission a 500 GHz receiver at the James Clerk Maxwell Telescope (JCMT), Hilo, HI, USA. In 1996, he joined the Herzberg Institute of Astrophysics, National Research Council Canada, Victoria, BC, Canada, where he continued development on low-noise receivers for astronomy, including a 200 GHz receiver for the JCMT and a sideband separating mixer design. From 2000 to 2002, he was with the Institut de Radioastronomie Millimétrique, Grenoble, France, where he was involved with the design of a 275–370 GHz receiver (Band 7) for the Atacama Large Millimetre Array. From 2002 to 2014, he led the Millimetre-Wave Instrumentation Group, NRC Herzberg Astronomy and Astrophysics, National Research Council Canada, Victoria, BC, Canada. He was the Project Engineer for the 84–116 GHz receiver (Band 3) developed for ALMA and was also an Adjunct Professor with the University of Victoria, Victoria, BC, Canada.